Available online at www.sciencedirect.com
SCIENCE DIRECT®
Journal of Sound and Vibration 277 (2004) 369–390
JOURNAL OF SOUND AND VIBRATION
www.elsevier.com/locate/jsvi

On noise reduction by flap side edge fences

Yueping Guo*

The Boeing Company, Mail Code H013-B308, 5301 Bolsa Avenue, Huntington Beach, CA 92647 USA

Received 30 April 2003; accepted 2 September 2003

Abstract

This paper discusses the effects of fences on side edge cross flows. Experimental data are reviewed to show that fences can modify the cross flow in the side edge region of aircraft flaps in such a way that noise reduction can be achieved. Near field pressure data reveal that fences reduce the characteristic frequency of the flow fluctuations. This leads us to postulate that the fences make the far field noise spectra shift downward in frequency. Because airframe noise spectra typically have a negative slope in the most important mid to high frequency domain, this downward shift in frequency leads to an equivalent reduction of noise levels, when measured by conventional metric such as the effective perceived noise level in aircraft certification. To explain the decrease of the characteristic frequency of the flow fluctuations due to the fences, an analytical model is developed, based on vortex dynamics. The predictions from the model are shown to be in very good agreement with measured data, both for the dominant frequency in the baseline case without the fences and for the trends of the decreasing frequency with increasing fence height.

1. Introduction

Flap side edge flows have long been recognized as a significant contributor to airframe noise. The noise source mechanisms are related to the vortex structure of the cross flows in the flap side edge region [1–5]. This understanding has led to noise reduction concepts such as flap side edge fences, which seek to modify the flow features of the vortex structure in a favorable way so that noise from these flows is reduced. While the application of this concept to real aircraft still faces practical difficulties, such as the added weight and cost, its effectiveness in reducing flap-related noise has been very clearly demonstrated [6–8]. These successful demonstrations include both simplified flaps and realistic aircraft configurations. Typically, side edge fences can achieve a noise reduction of up to 4 dB in the middle to high frequency domain in which flaps are known to be

*Tel.: +1-714-8961527; fax: +1-714-8961559.
E-mail address: yueping.guo@boeing.com (Y. Guo).

0022-460X/$ - see front matter © 2003 Elsevier Ltd. All rights reserved.
doi:10.1016/j.jsv.2003.09.029

major noise sources. In this paper, we discuss the mechanisms that cause this reduction and present an analytical model for studying these mechanisms.

Flap side edge fences are simple devices; they are basically flat plates attached to the side surfaces of the flaps in such a way that the plates protrude into the flow on the lower side of the flaps. It has been confirmed in wind tunnel tests that the fences only change the local flows in that the overall lift characteristics of the flaps and the high lift systems is not affected by the fences in any significant way [7]. In fact, this is a fundamental requirement for any noise reduction device; it should not significantly affect the aerodynamic performance of the high lift systems.

With such a device, the noise reduction comes from the modification of the local flow structures. To show this, some experimental data will be reviewed. It will be shown that the most noticeable feature in the near field flow is the decrease of the characteristic frequencies of the flow fluctuations. The vortex structure in the cross flow manifests itself in the surface pressures in the form of distinct spectral humps [9]. When fences are applied, the dominant frequencies of the humps are reduced, which will be shown both in the spectra and in the cross coherence of the surface pressures. The decrease in the dominant frequencies in the near field flow is also accompanied by a decrease in the dominant frequencies in the far field noise. This will be demonstrated by the near field/far field coherence, showing a progressive downward shift of the peak coherence frequencies, as the fence height increases.

This leads us to postulate that noise reduction due to fences may at least partially come from a downward shift of the noise spectra in the frequency domain. It is known that the spectra of flap-related noise typically have a negative slope in the middle and high frequency domain where the noise levels are heavily weighted for the purpose of aircraft noise certification. Thus, a downward shift of the spectra in frequency lowers the spectral levels in any fixed frequency bands in the middle to high frequency domain. The spectrum shift will also increase the noise levels at frequencies below the peak frequency where the spectra have a positive slope, which will also be shown by some measured data. The increase in low frequency noise is, however, less important for aircraft noise certification, because the low frequency components are lightly weighted in the noise metrics for certification, such as the effective perceived noise level (EPNL).

Obviously, it is also possible that the fences may modify the local flow so that the amplitudes of the flow fluctuations are reduced, which may in turn result in a reduction of far field noise. The measured data we have, however, are not detailed enough to resolve this issue and further investigation is needed.

To explain the downward frequency shift of the local source process when fences are applied, an analytical model will be developed, based on vortex dynamics. The basic assumption here is that the side edge flow is dominated by a vortex structure, which is consistent with results from recent CFD computations [10] and measurements from small-scale idealized experiments [11], as well as previous modelling efforts [1–5]. To establish the model for the oscillations of this side edge vortex structure, the flow is approximated as incompressible with viscosity confined to concentrated vortex cores. This approach is applicable here because the flows have low Mach numbers and very high Reynolds numbers; at approach conditions for commercial aircraft where flap-related noise is important, the flow Mach numbers are typically between 0.2 and 0.3.

By making use of a local two-dimensional approximation, the technique of conformal mapping, together with the application of vortex dynamics, is used to derive analytical solutions for the oscillation frequencies of the local flow. The frequencies depend on the local flap/fence geometry

and the strength of the vortex, which can be determined from the imposition of the Kutta condition at the sharp corners of the side surface. The model will then be used to predict the dominant frequencies of local flow oscillations for a 4.7% DC-10 aircraft, for which experimental data are available. The comparison between predictions and data show very good agreements, not only in the trends of decreasing frequency with increasing fence height, but also in the absolute values of the peak frequencies.

It is appropriate to point out that, though flap fences have been observed to be able to achieve quite noticeable noise reduction, there are still practical issues to be resolved before their implementation on commercial airplanes. One of them is the added weight and cost. These issues become even more severe when considering the reduced benefit of the fences for the total airframe noise, which consists of many other components not affected by the fences. For noise exclusively from flap side edges, fences can achieve a reduction of about 4 dB for the EPNL, but the reduction in EPNL dB can be expected to be much less for the total airframe noise. This is especially true for cases where other sources, such as those related to the slats and landing gears, are equally or more important but basically unaffected by flap fences. This is indeed the case for modern commercial airplanes, which tend to have fewer flap elements and lower flap deployment angles, because of advanced high lift system design. This reduces the relative importance of flap-related noise sources, and thus, reduces the benefit of any flap noise reduction devices, including the fences.

2. Experimental observations

To demonstrate the effects of fences on flap side edge flows and their noise radiation, this section presents some data obtained from an acoustic test in the facility of the NASA Ames 40 ft × 80 ft wind tunnel, which is a closed flow facility with partial acoustic treatment. The test was done for a 4.7% small-scale model of the McDonnell Douglas DC-10-30 transport airplane. Both far field noise and near field surface pressure measurements were made for various flow conditions and high lift system configurations. Details of this test have been previously reported [8,12] so that only data relevant to flap side edge fences are discussed here. Three flap fences or differing heights were studied in the test. The smallest of the three has a height of half the maximum flap thickness and the other two have heights, respectively, equal to one and two maximum flap thickness. In all the discussions in this paper, the fence height will be normalized by the half thickness of the baseline flap and the non-dimensional fence height will be denoted by h. Thus, the four cases (baseline plus three fences) are, respectively, represented by h=0,1,2,4. For the studies of flap fences, the free stream flow Mach number in the test is 0.275 and the wing angle of attack is fixed at 5° with landing gears retracted. The flaps are deployed at a fixed angle of 50°, but the slats are varied with two settings, one at 20° and the other being retracted.

The noise reduction by flap fences is demonstrated in Figs. 1 and 2. Fig. 1 plots the noise spectra in 1/3-octave bands (dB re 20 μPa) at a microphone location 1.22 m (4 ft) below the outboard edge of the outboard flap on one wing, 83° from the upstream direction. The directivity angle and distance are set to mimic the fly over location in aircraft noise certification test. Both cases with and without fences are shown in the figure. All cases are for Mach number of 0.275, flaps and slats, respectively, deployed at 50° and 20° and landing gear retracted. Flap side edge fences are shown here to be effective for frequencies above about 1000 Hz, which corresponds to a

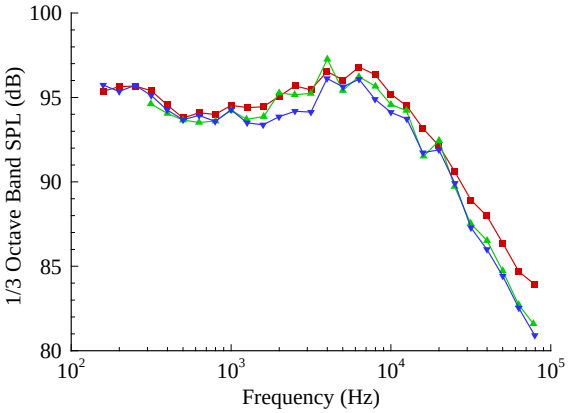

Fig. 1. Noise reduction by flap side edge fences with Mach number $M = 0.275$, flap and slat, respectively, deployed at 50° and 20° and landing gear retracted. The measurement microphone is 4 ft below the wing (84° from upstream direction). -■-, no fence; -▲-, $h = 2$; -▼-, $h = 4$.

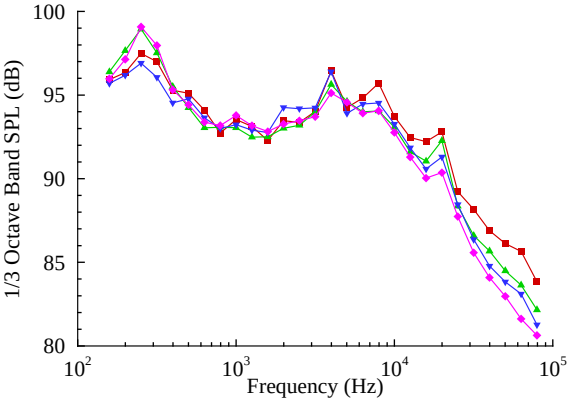

Fig. 2. Noise reduction by flap side edge fences. The high lift system configurations and flow conditions are the same as those for Fig. 1, expect that the slat is retracted. -■-, no fence; -▲-, $h = 1$;-▼-, $h = 2$; -◆-, $h = 4$.

frequency of about 50 Hz for full-scale aircraft, because the model used in the tests is 4.7%. Thus, fences reduce flap-related noise essentially in the entire frequency band of interest to aircraft noise certification. The average reduction for the case shown in Fig. 1 is about 2 dB. The effectiveness of the fences slightly improves at high frequencies because noise from the DC-10 aircraft model is dominated by flap-related sources, which is mainly in the high frequency domain.

The noise reduction of about 2 dB shown in Fig. 1 does not completely demonstrate the effectiveness of the fences because the high lift system configuration includes slat deployment at 20°. The noise form the slat, which is not affected by the fences, may act as a noise floor, limiting the amount of reduction in the total noise. To demonstrate this, Fig. 2 shows some results for the case where all the test conditions are the same as those for Fig. 1, except that the slat is retracted so that the noise can be regarded as from the flaps alone. It is clear from this figure that the amount of noise reduction can be as high as 4 dB for this DC-10 model, about doubling the

amount when the slat is deployed. The trends due to the different fence heights are also clear in this figure. For the three fences tested, it seems that large fences have the most noise reduction. However, the amount of noise reduction does not increase linearly with the fence height. From the case without fence to that with the half thickness fence, a significant reduction is achieved. As the fence height increases, the increase in noise reduction becomes very gradual; doubling the fence height from one to two flap-thickness does not seem to yield much benefit. From the noise spectra at all far field angles, the radiated noise can be calculated in terms of EPNL, which is an important metric in aircraft noise certification. For the cases shown in Fig. 2, the reduction in EPNL is about 4 dB. This is clearly quite significant. It is, however, appropriate to point out that the reduction is for flap-related noise only. In practical application of total aircraft noise consisting of many other components, the reduction in total EPNL dB can be expected to be much less. This is especially true for cases where the flaps are not the dominant sources. An example is new commercial airplanes developed in recent years, such as the Boeing 777, which have fewer flap elements and relatively lower flap settings. In this case, the total airframe noise may not be very sensitive to flap side edge treatments such as the fences.

It is of interest to note from Fig. 2 that, while the fences are effective in reducing high frequency noise, they actually increase the noise level at low frequencies. For example, the case with the two-thickness fence (the curve with diamonds in Fig. 2) has higher noise level at low frequencies than all other cases, including that without fence. This dual effect of the fences, namely, reducing high frequency noise and increasing low frequency noise, may be explained by a downward shift of the dominant frequency in the source mechanisms. Since typical flap noise spectra have a broad peak at the dominant frequency and falls off on both sides of the peak, a downward shift of the peak due to the fences would make the high frequency part appear as a reduction in spectral levels. Similarly, the levels in the low frequency part of the spectra would appear to be increased due to the shift. Thus, even without any reduction in source strength, a downward shift in frequency may appear as a noise reduction because flap-related noise is dominated by high frequency components, which are also most sensitive and are heavily weighted for aircraft noise certification. It should be pointed out that the far field noise measurements themselves do not enable us to conclusively show whether there is a weakening in source strength due to the fences, which may also contribute to the observed reduction in far field noise. The data plotted in Fig. 2, however, suggest that the mechanism of a downward frequency shift in the source process may play a role in reducing the flap-related noise.

This frequency shift due to the fences can be more clearly seen in the near field surface pressure measurements [9]. These measurements were done in the test at the outboard edge of the outboard flap, on both the lower and the upper surfaces, as well as on the side surface. The locations of the surface pressure sensors are shown in Fig. 3. Results from two of the sensors, denoted by SP19 and SP21 in Fig. 3, are shown in Figs. 4 and 5. Both sensors are 0.635 cm (1/4 in) away from the side edge. SP21, which is on the upper surface, is 1/4 flap chord upstream of the flap trailing edge and SP19, the lower surface sensor, is at the mid chord location. The locations of the surface pressure sensors are chosen such that they are close to the vortex structure in the flow. Thus, the sensors capture the dominant features of the vortex flow. The test conditions for the results shown in Figs. 4 and 5 are the same as those for Fig. 2. The most noticeable features in both Figs. 4 and 5 are the distinctive spectral humps, which can be attributed to the evolution of the vortex structure in the flap cross flow [9]. Clearly, the effects of the vortex structure are present for both unfenced

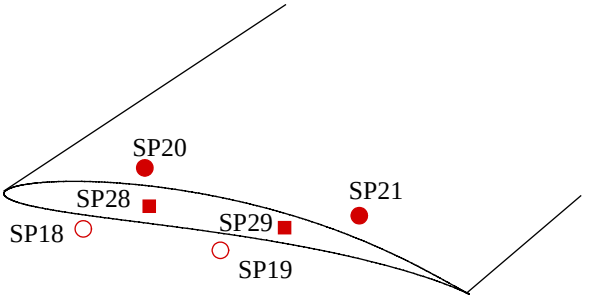

Fig. 3. Locations of surface sensors for measuring pressure fluctuations at the outboard edge of the outboard flap. Results from SP21 and SP19 are, respectively, shown in Figs. 4 and 5. ●, Upper surface; ■, side surface; ○, lower surface.

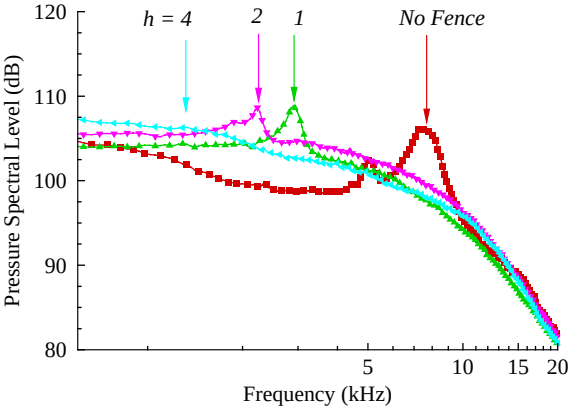

Fig. 4. Surface pressure spectra at the lower surface sensor SP19 for various fences, showing the progressive decrease of the hump frequency with increasing fence height. -■-, no fence; -▲-, $h = 1$; -▼-, $h = 2$; -◀-, $h = 4$.

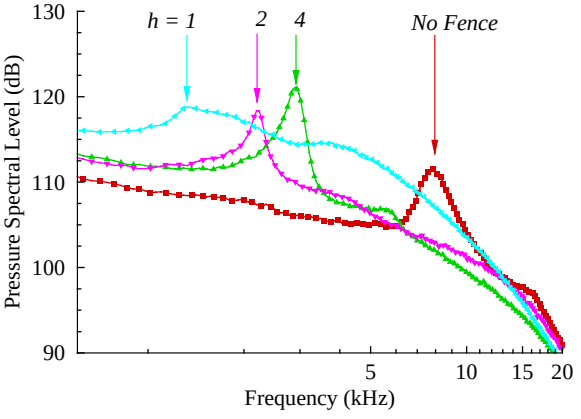

Fig. 5. Surface pressure spectra at the upper surface sensor SP21 for various fences, showing the progressive decrease of the hump frequency with increasing fence height. -■-, no fence; -▲-, $h = 1$; -▼-, $h = 2$; -◀-, $h = 4$.

and fenced flaps, as indicated by the presence of the spectral humps in all cases. It is interesting to note that the peaks of the spectral humps shift to lower frequencies as the fence height increases.

As can be expected, the lower peak frequencies in the surface pressure spectra when fences are applied also manifest themselves in the coherence of the near field quantities, which is illustrated in Fig. 6, by the coherence coefficient between the two measurements shown in Figs. 4 and 5. Without the fences, a high coherence coefficient of about 0.8 is seen at about 7.5 kHz, the same frequency as the spectral humps in Figs. 4 and 5 for the corresponding case. This of course indicates that the vortex structure, which is the cause of the spectral humps, is the most coherent feature in the flap cross flow. When the fences are applied and as the fence height increases, the vortex structure remains highly coherent, but the peak frequency of the coherence coefficient gradually decreases, again, confirming the downward frequency shift of the source process when fences are applied. It can also be noticed, in Figs. 4–6, that the decrease in peak frequency is not linearly proportional to the increase of the flap fence height.

The changes in the near field flow due to the side edge fences also affect the sound/surface pressure coherence. This is shown in Fig. 7, which plots the coherence coefficient between noise measurements in the far field, as shown in Fig. 2, and the surface pressure measurements on the lower surface of the flap, given in Figs. 4 and 5. The bottom diagram of Fig. 7 is for the case without fence, which shows a maximum in the coherence coefficient at about 7.5 kHz, precisely the same frequency as the spectral humps in the surface pressures in Figs. 4 and 5 for the corresponding unfenced flap. This clearly reveals the cause-and-effect relation between the near field vortex structure and the far field radiation. The next diagram up in Fig. 7 is for the smallest fence that has a height of half the flap thickness. For this fence, the peak frequency of the sound/surface pressure coherence is shifted from 7.5 kHz for the case without fences downward to about 3 kHz, and the width of the coherence peak is also reduced. These trends continue as the fence height increases from half flap thickness to one flap thickness and finally to twice the flap thickness, shown by the top diagram in Fig. 7. For the largest fence, the side edge fences essentially suppress the coherence, though the maximum can still be seen well above the incoherent background.

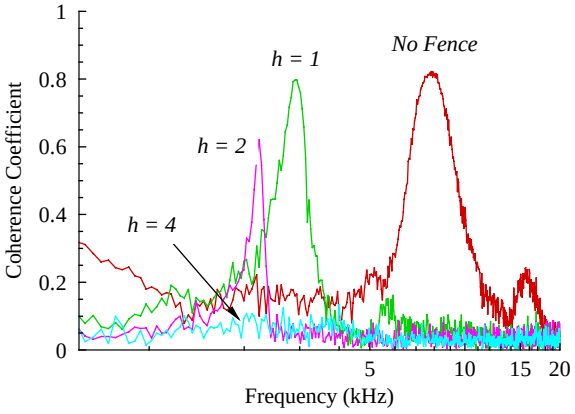

Fig. 6. Effects of different flap fences on the cross coherence between two sensors, respectively, on the upper and lower flap surface. The spectra of the two sensors are shown in Figs. 4 and 5. The fences shift the peak frequency downwards, as well as reducing the amplitude and width of the coherence.

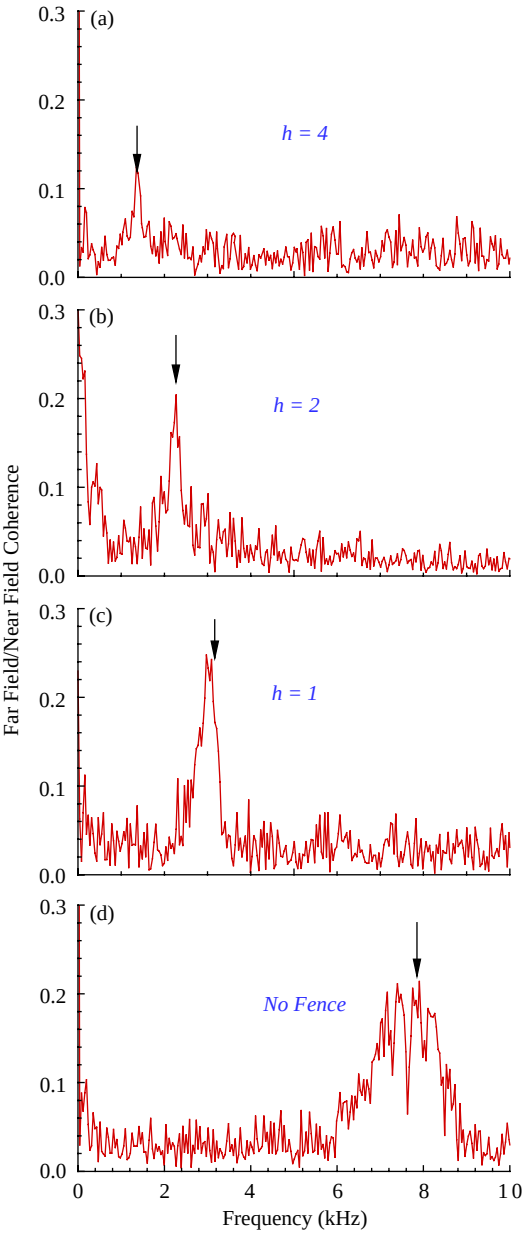

Fig. 7. Coherence between far field sound and unsteady surface pressure on the flap lower surface for different flap fences, showing the downward shift of the peak coherence frequency with fence height.

3. Model for flap side edge fence

To model the flap side edge fence, we follow previous studies [1,4] to adopt a locally two-dimensional near field model. In this model, the fully three-dimensional roll-up vortex flow,

as illustrated in Fig. 8, is divided into strips in the chord-wise mean flow direction. Each strip is then approximated as two-dimensional. This local approximation is also illustrated in Fig. 8; at any fixed chord-wise location, the A-A section in Fig. 8, for example, the geometry reduces to two-dimensional. This local geometry is illustrated in Fig. 9, together with the dimensions of the flap and the fence. It is convenient to work with non-dimensional quantities. To this end, we choose the half thickness of the flat, b, as the length scale and use it to normalize all length quantities and co-ordinates. The co-ordinate system (x, y) is also shown in this figure, whose center is located at the middle point of the flap thickness. We denote the height of the fence by h and its thickness by s. Thus, the surfaces of the flap can be specified as

$$y = \pm 1, \quad -\infty < x \leqslant 0 \tag{3.1}$$

and the surfaces of fence is defined by

$$-s \leqslant x \leqslant 0, \quad -(1+h) \leqslant y \leqslant -1. \tag{3.2}$$

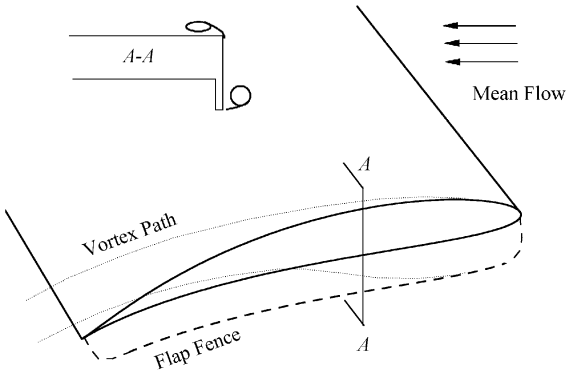

Fig. 8. Illustration of the flap side edge flow and the local geometry of the fenced flap.

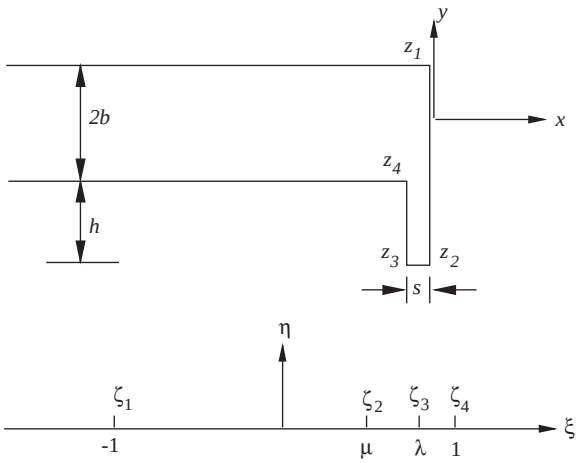

Fig. 9. Flap local geometry and its conformal mapping to a semi-infinite plane.

In practical applications, the fence thickness is usually much smaller than that of the flap, namely, $s \ll 1$.

The two-dimensional approximation of the local geometry clearly suggests the use of conformal mapping; the Schwartz–Christoffel transformation can be used to map the flow region in the physical plane to the upper half of a mathematical plane. The co-ordinates in the two mapping planes are, respectively, z and ζ, defined by

$$z = x + \mathrm{i}y \quad \text{and} \quad \zeta = \xi + \mathrm{i}\eta. \tag{3.3}$$

To illustrate, the correspondence of the two planes is shown in Fig. 9 where the vertices of the flap side edge are denoted by z_n with $n = 1,2,3,4$. The corresponding points in the mapping plane are given by ζ_n, of which two can be arbitrarily specified and the other two are to be determined by the mapping relation. We choose to map the points $z = \mathrm{i}$ and $z = -s - \mathrm{i}$ to $\zeta = \pm 1$ so that the relations of the individual points in these two planes can be summarized as

$$\begin{array}{lccccc} z_n = & \mathrm{i} & -\mathrm{i}(1+h) & -s-\mathrm{i}(1+h) & -s-\mathrm{i}, \\ \zeta_n = & -1 & \mu & \lambda & 1. \end{array} \tag{3.4}$$

Here μ and λ are two real constants to be determined. They are the two points in the mapping plane, which correspond to the two corners of the fence in the physical plane. With this choice of the vertices, the Schwartz–Christoffel transformation can be written as

$$\frac{\mathrm{d}z}{\mathrm{d}\zeta} = z'(\zeta) = a\left(\frac{(\zeta+1)(\zeta-\mu)(\zeta-\lambda)}{\zeta-1}\right)^{1/2}, \tag{3.5}$$

where a is constant to be determined and the prime over z indicates differentiation with respect to ζ.

Transformation (3.5) can be integrated in terms of elliptic functions. The result contains four constants to be determined, namely μ, λ, a and an integration constant. These constants can be found by using Eq. (3.4). In particular, two equations can be derived to determine the two real constants μ and λ. These are

$$sf_1(\mu,\lambda) - (1+h)f_2(\mu,\lambda) = 0, \quad sf_3(\mu,\lambda) - hf_1(\mu,\lambda) = 0, \tag{3.6}$$

where f_1, f_2 and f_3 are introduced to denote the real-valued integral

$$\int \sqrt{(\xi+1)|(\mu-\xi)(\lambda-\xi)|/(1-\xi)}\,\mathrm{d}\xi \tag{3.7}$$

with the vertical bars meaning absolute values. The lower and upper limits for the three integrals are given by

$$\begin{array}{lccc} & f_1 & f_2 & f_3 \\ \text{Upper limit} & \mu & \lambda & 1 \\ \text{Lower limit} & -1 & \mu & \lambda \end{array} \tag{3.8}$$

The two equations (3.6) can be solved numerically to find μ and λ as functions of s and h. It is also convenient to calculate the straightforward integrals defined by Eqs. (3.7) and (3.8), for given μ and λ. This way, s and h are expressed as functions of μ and λ. The results are shown in Fig. 10, plotted in the μ–λ plane as constant s and h contours. It can be noted that the values of μ and λ are

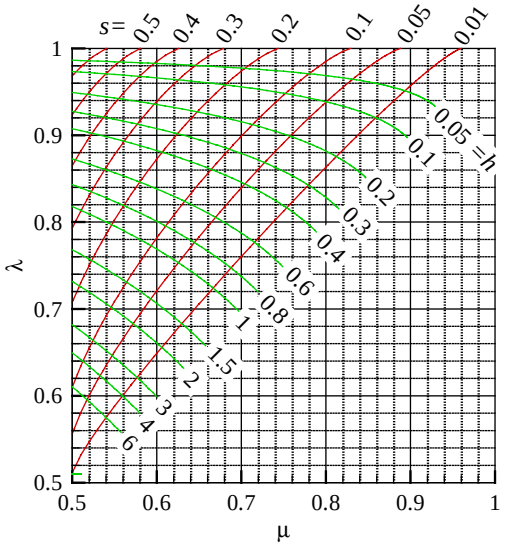

Fig. 10. The parameter λ and μ, as functions of the flap fence height h and fence thickness s.

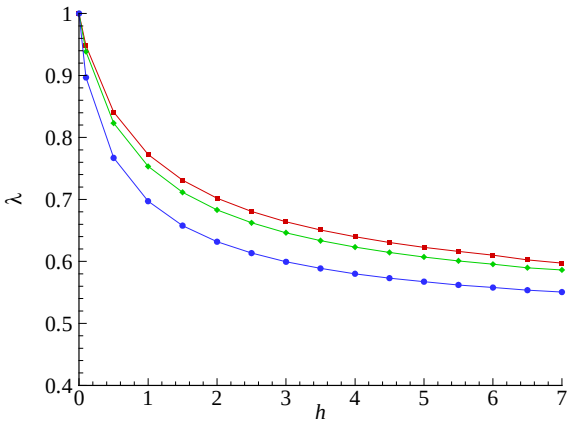

Fig. 11. The location of the fence edge z_3 in the complex ζ-plane as a function of the non-dimensional fence height for three values of fence thickness. -■-, $s = 0.1$; -◆-, $s = 0.05$; -●-, $s = 0$.

confined to the triangular domain bounded between 0.5 and 1. The domain has a triangular shape because λ is always larger than μ (see Fig. 9), while it is bounded between 0.5 and 1 because both μ and λ approach unity as h approaches zero and both limit to 0.5 when h is very large. Some results are also shown in Figs. 11 and 12, for μ and λ, as a function of the fence height h, for three values of the fence thickness s. These two parameters are the locations of the fence edges z_2 and z_3 in the complex mapping plane.

With all the constants determined, the mapping can then be written as

$$z = aF(\zeta) + \mathrm{i}, \tag{3.9}$$

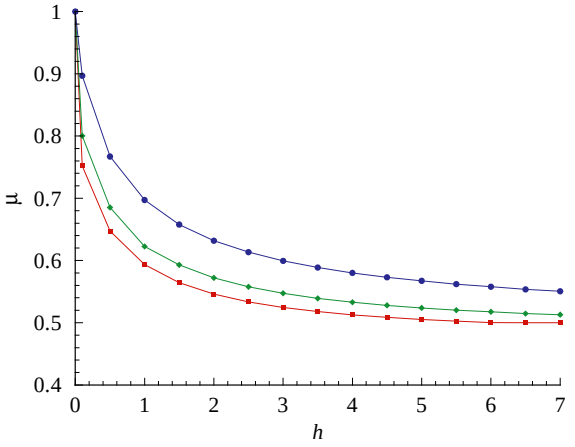

Fig. 12. The location of the fence edge z_2 in the complex ζ-plane as a function of the non-dimensional fence height for three values of fence thickness. -■-, $s = 0.1$; -◆-, $s = 0.05$; -●-, $s = 0$.

where a is given by

$$a = -(2 + h)/f_1 \tag{3.10}$$

with f_1 defined by the integral (3.7) with its lower and upper integration limit given by Eq. (3.8). The complex function $F(\zeta)$ in Eq. (3.9) is defined by

$$F(\zeta) = \int_{-1}^{\zeta} \left(\frac{(\zeta + 1)(\zeta - \mu)(\zeta - \lambda)}{\zeta - 1} \right)^{1/2} \mathrm{d}\zeta. \tag{3.11}$$

Under this mapping, the surfaces of the semi-infinite plate with the attached fence, given by Eqs. (3.1) and (3.2), is projected onto the real axis $\eta = 0$ in the complex ζ-plane.

4. Vortex motion

We consider the situation where the flap/fence system is embedded in a potential cross flow that is characterized by a velocity U. It is the uniform mean flow velocity in the transformed complex ζ-plane in the negative ξ direction. This velocity is used as the reference velocity, but is otherwise not related to any physically meaningful parameters. The advantage of the mapping from the z-plane to the ζ-plane is that the complex potential in the latter plane can be very easily found to be that due to a uniform flow plus contributions from all the vortices in the flow. We denote the trajectory of the vortex in the physical plane by $z_k(t)$, where t is the non-dimensional time (the reference time being b/U). The vortex trajectory is mapped to the complex ζ-plane through Eq. (3.9), and will be denoted by $\zeta_k(t)$. This leads to simple mathematical forms for the complex potential in the ζ-plane, which is normalized by Ub and is denoted by W,

$$W(\zeta, t) = -\zeta + \frac{\Gamma_k}{2\pi \mathrm{i}} \ln \frac{\zeta - \zeta_k}{\zeta - \zeta_k^*}, \tag{4.1}$$

where the vortex has non-dimensional strength Γ_k (normalized by Ub) and the superscript $*$ indicates complex conjugate. According to the theory of potential flows, the velocities u and v in the physical z-plane, respectively, in the x and y direction, can be derived from the complex potential (4.1) by

$$\frac{u-\mathrm{i}v}{U}=\frac{\mathrm{d}W}{\mathrm{d}z}=\frac{\mathrm{d}W}{\mathrm{d}\zeta}\frac{\mathrm{d}\zeta}{\mathrm{d}z}=\frac{1}{z'(\zeta)}\frac{\mathrm{d}W}{\mathrm{d}\zeta}, \tag{4.2}$$

where z' is given by Eq. (3.5), and $\mathrm{d}W/\mathrm{d}\zeta$ can be easily found from Eq. (4.1) as

$$\frac{\mathrm{d}W(\zeta)}{\mathrm{d}\zeta}=-1+\frac{\Gamma_k}{2\pi\mathrm{i}}\left(\frac{1}{\zeta-\zeta_k}-\frac{1}{\zeta-\zeta_k^*}\right). \tag{4.3}$$

To determine the motions of the vortices, we can follow the Roth rule by requiring that the velocity of a vortex at any given time is given by the regular part of the local flow velocity at the location of the vortex at that time. Mathematically, this is expressed as

$$\frac{\mathrm{d}z_k}{\mathrm{d}t}=\lim_{z\to z_k}\left(\frac{\mathrm{d}W}{\mathrm{d}z}-\frac{\Gamma_k}{2\pi\mathrm{i}}\frac{1}{z-z_k}\right)^*, \tag{4.4}$$

where $\mathrm{d}z_k/\mathrm{d}t$ is the velocity at which the vortex moves. The first term in the brackets under the limiting process is the total local flow velocity, given by Eq. (4.2), while the second is the singular contribution of the vortex at its instantaneous location. On inspection of Eq. (4.3), it is clear that the only singular part in $\mathrm{d}W/\mathrm{d}z$ as $z\to z_k$ comes from the first term under the summation in Eq. (4.3) when $\zeta\to\zeta_k$. Thus, for other terms, the limiting process $z\to z_k$, which is equivalent to $\zeta\to\zeta_k$, is simply the substitution of ζ by ζ_k. For the remaining terms, we have the limiting operation

$$\begin{aligned}\lim_{\zeta\to\zeta_k}\left(\frac{1}{z'(\zeta)}\frac{1}{\zeta-\zeta_k}-\frac{1}{z-z_k}\right)&=\frac{1}{z'(\zeta_k)}\lim_{\zeta\to\zeta_k}\left(\frac{z-z_k-z'(\zeta)(\zeta-\zeta_k)}{(\zeta-\zeta_k)(z-z_k)}\right)\\&=\frac{1}{2z'(\zeta_k)}\frac{z''(\zeta_k)}{z'(\zeta_k)},\end{aligned} \tag{4.5}$$

where $z''(\zeta)$ is the second order derivative of z with respect to ζ, which can be derived by differentiating Eq. (3.3)

$$z''(\zeta)=\frac{a}{2}\frac{(\zeta^2-1)(2\zeta-\mu-\lambda)-2(\zeta-\mu)(\zeta-\lambda)}{(\zeta-1)(\zeta^2-1)^{1/2}(\zeta-\mu)^{1/2}(\zeta-\lambda)^{1/2}}. \tag{4.6}$$

On collecting all the results above, it is easy to show that Eq. (4.4) can be written as

$$\frac{\mathrm{d}z_k^*}{\mathrm{d}t}=\frac{1}{z'(\zeta_k)}\left(-1+\frac{1}{4\pi}\Gamma_k(\eta_k^{-1}+\mathrm{i}\beta(\zeta_k))\right), \tag{4.7}$$

where η_k is the imaginary part of ζ_k and the quantity β is introduced to denote

$$\beta=\frac{z''}{z'}=\frac{1}{2}\left(\frac{1}{\zeta-\mu}+\frac{1}{\zeta-\lambda}-\frac{2}{\zeta^2-1}\right). \tag{4.8}$$

Since the right-hand side of Eq. (4.7) involves only quantities in the ζ-plane, it is convenient to convert its left-hand side, namely, the velocity of the vortex at z_k in the physical plane, to its

counterpart in the ζ-plane. This is done by the application of the chain rule of differentiation,

$$\frac{\mathrm{d}\zeta_k}{\mathrm{d}t} = \frac{\mathrm{d}\zeta_k}{\mathrm{d}z_k}\frac{\mathrm{d}z_k}{\mathrm{d}t} = \frac{1}{z'(\zeta_k)}\frac{\mathrm{d}z_k}{\mathrm{d}t}. \tag{4.9}$$

On substituting Eqs. (4.7) and (3.3) into this, we have

$$\frac{\mathrm{d}\zeta_k^*}{\mathrm{d}t} = \frac{1}{|z'(\zeta_k)|^2}\left(-1 + \frac{1}{4\pi}\Gamma_k(\eta_k^{-1} + \mathrm{i}\beta(\zeta_k))\right), \tag{4.10}$$

where the vertical bars mean absolute value.

From the motions of the vortices, the velocity field can be found by using Eqs. (4.2) and (4.3). It is also straightforward to calculate the pressure fluctuations in the flow. This can be done through the Bernoulli equation,

$$\frac{p_0 - p}{q} = 2\mathrm{Re}\left(\frac{\mathrm{d}W}{\mathrm{d}t}\right) + \left|\frac{\mathrm{d}W}{\mathrm{d}z}\right|^2, \tag{4.11}$$

where p is the total pressure, p_0 denotes the static pressure at infinity and q stands for the dynamic head of the reference flow defined by

$$q = \tfrac{1}{2}\rho_0 U^2 \tag{4.12}$$

with ρ_0 being the constant mean density. Of particular interest is the pressure fluctuation on the flap/fence surfaces, which we denote by p_s. In terms of the vortex trajectory ζ_k, the surface pressure can be written as

$$\frac{p_s - p_0}{q} = \frac{2}{\pi}\Gamma_k\,\mathrm{Im}\left(\frac{\mathrm{d}\zeta_k/\mathrm{d}t}{\xi - \zeta_k}\right) - \frac{1}{|z'(\xi)|^2}\left|1 + \frac{1}{\pi}\Gamma_k\,\mathrm{Im}\left(\frac{1}{\zeta_k - \xi}\right)\right|^2, \tag{4.13}$$

where we have made use of the fact that the quantity ζ is real and equal to ξ on the surfaces defined by Eqs. (3.1) and (3.2).

5. Small amplitude oscillations

Eq. (4.10) describes the motions of the vortices. In general, there is a vortex in the side edge region that moves around an equilibrium position. The equilibrium positions can be found by setting the right-hand side of Eq. (4.10) to zero. By denoting the vortex quantities in equilibrium by the subscript "0", we have

$$\frac{8\pi\mathrm{i}}{\Gamma_0} - \frac{2\mathrm{i}}{\eta_0} + \frac{1}{\zeta_0 - \mu} + \frac{1}{\zeta_0 - \lambda} - \frac{2}{\zeta_0^2 - 1} = 0. \tag{5.1}$$

For given values of s and h, the parameters μ and λ are uniquely determined by Eq. (3.6). Thus, the only parameter that has to be specified, in order to find ζ_0 from Eq. (5.1), is the non-dimensional vortex strength Γ_0. This quantity can be determined by the Kutta condition, namely, by requiring the velocity at the corners to be always finite. The velocity (4.2) from potential flow theory becomes singular at the sharp corners because z' approaches zero when ζ approaches the points in the mapped plane, which correspond to the corners in the physical plane. For example,

the corner on the upper flap surface are given by

$$z_e = \mathrm{i} \quad \text{and} \quad \zeta_e = \mu. \tag{5.2}$$

It is clear that finite velocities are achieved at the corners only if

$$\frac{\mathrm{d}W(\zeta)}{\mathrm{d}\zeta} = 0 \quad \text{at } \zeta = \zeta_e. \tag{5.3}$$

This is in fact the mathematical expression for the Kutta condition for the problem considered here. With $\mathrm{d}W/\mathrm{d}\zeta$ given by Eq. (4.3), this condition becomes

$$\Gamma_0 \mathrm{Im} \frac{1}{\zeta_e - \zeta_0} = \pi. \tag{5.4}$$

By combining Eqs. (5.1) and (5.4), a single equation can be derived to find the vortex equilibrium location in the ζ-plane. The result can then be mapped by Eq. (3.9) to find the locations of the static vortex in the physical plane. Some results are plotted in Fig. 13; the ζ values of the equilibrium location are shown, as a function of the fence height h, for three values of the fence thickness s. The equilibrium positions vary noticeably with the fence height, but are not significantly affected by the fence thickness.

Once the equilibrium position of the vortex is found, we can examine its small amplitude oscillations by linearizing the governing equation (4.10). To this end, we write

$$\zeta_k = \zeta_0 + \varepsilon(t), \tag{5.5}$$

where $\varepsilon = \varepsilon_r + \mathrm{i}\varepsilon_i$ is the time-dependent perturbation of the vortex trajectory. By substituting this into Eq. (4.10), we can expand all quantities in terms of ε. For example,

$$\beta(\zeta_k) = \beta(\zeta_0) + \varepsilon\beta'(\zeta_0), \tag{5.6}$$

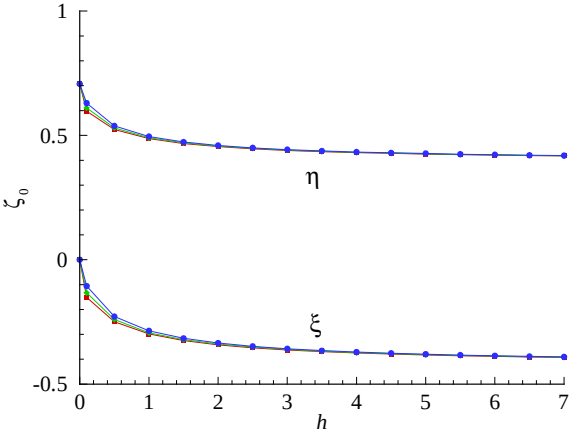

Fig. 13. Locations of the equilibrium vortex in the complex ζ-plane, as a function of the flap fence height for three values of the fence thickness. -■-, $s = 0.1$; -◆-, $s = 0.05$; -●-, $s = 0$.

where terms of the order ε^2 or higher have been neglected and β' is given by

$$\beta' = \frac{1}{2}\left(\frac{4\zeta_0}{(\zeta_0^2-1)^2} - \frac{1}{(\zeta_0-\mu)^2} - \frac{1}{(\zeta_0-\lambda)^2}\right). \tag{5.7}$$

By expanding all terms in Eq. (4.10) and grouping terms of the same order in ε, it is easy to show that the zeroth order terms cancel each other because of Eq. (5.1). The first order terms lead to

$$\frac{\mathrm{d}\varepsilon^*}{\mathrm{d}t} = \frac{\Gamma_0}{4\pi|z'|^2}\left(\frac{\mathrm{i}\varepsilon_i}{\eta_0^2} + \varepsilon\beta'\right), \tag{5.8}$$

where z' is given by Eq. (3.5). This is an ordinary differential equation in time with constant coefficient. It can be very easily re-written in the familiar form

$$\frac{\mathrm{d}^2\varepsilon}{\mathrm{d}t^2} + \omega^2\varepsilon = 0 \tag{5.9}$$

with the angular frequency defined by

$$\omega = \frac{\Gamma_0}{4\pi|z'|^2}(-|\beta'|^2 - \mathrm{Re}(\beta')/\eta_0^2)^{1/2}. \tag{5.10}$$

This result gives the non-dimensional frequencies of the vortex oscillations and can be used to study the trends of the frequencies as a function of the fence height and to predict the hump frequencies discussed in Section 2.

6. Comparison with data

We start with the baseline case without fences. In this event, $h=0$ and both μ and λ are equal to unity. Eqs. (5.1) and (5.4) then reduce to very simple forms and it is easy to show that the equilibrium vortex is now specified by

$$\zeta_0 = \mathrm{i}/\sqrt{2} \quad \text{and} \quad \Gamma_0 = 3\pi/\sqrt{2}, \tag{6.1}$$

which leads to

$$z_0 = (\sqrt{3} + \ln(2+\sqrt{3}) + \ln 4)/\pi. \tag{6.2}$$

By substituting these results into (5.10) and denoting the oscillation frequency for the baseline case by f_0, we have

$$f_0 = (\pi\sqrt{2}/192)(U_0/b), \tag{6.3}$$

where the frequency is dimensional (Hz) and U_0 is the value of U in the baseline case of $h=0$.

It can be noted that though the problem formulated in the previous sections are uniquely determined in terms of the non-dimensional quantities, it is necessary to introduce empirical formula to specify U_0, in order to make estimate of the physical frequencies. As mentioned in Section 4, the parameter U_0 is used in the formulation only for the purpose of normalization. It may not necessarily be related to any physically meaningful quantities. Thus, instead of trying to interpret the physical meaning of U_0, we choose to determine its value through the vorticity of the

vortex, which is a physically measurable quantity. This can be done because U_0 is also used in the normalization of the vortex strength.

In dimensional quantities, the second result in Eq. (6.1) can be re-written as

$$\gamma_0 = (3\pi/\sqrt{2})U_0 b, \tag{6.4}$$

where γ_0 is the vortex strength in dimensional unit. This quantity can be estimated by the lift line theory. Here, it is assumed that the side edge vortex is convected downstream by the chord-wise mean flow to form part of the vortical wake behind the aircraft high lift system. According to the lift line theory, the amplitude of the vortical wake at any span-wise location is determined by the change in sectional lift at that location. Thus, we can write

$$\gamma_0 = 2LU_\infty \Delta C_L, \tag{6.5}$$

where L is the semi-span of the aircraft wing, U_∞ is the chord-wise mean flow velocity and ΔC_L is the jump in sectional lift coefficient over a span-wise distance equal to the flap thickness and centered at the flap side edge location. By equating Eqs. (6.5) and (6.4), we then have

$$U_0/U_\infty = (2\sqrt{2}/3\pi)(L/b)\Delta C_L \tag{6.6}$$

for the reference velocity U_0 and the frequency prediction (6.3) becomes

$$f_0 = (\Delta C_L/144)(U_\infty/b)(L/b). \tag{6.7}$$

This gives the oscillation frequency in terms of the geometry of the aircraft high lift system, the mean flow velocity and the sectional lift coefficient, all being physically measurable quantities and easily available either by experiments or numerical calculations.

For the case discussed in Section 2, namely, for a 4.7% DC-10 aircraft model, a typical sectional lift coefficient distribution is plotted in Fig. 14, which are from surface pressure measurements in the test described in Section 2. The mean flow Mach number for this case is 0.275, yielding

$$U_\infty = 93.5\,\mathrm{m}^2/\mathrm{s}. \tag{6.8}$$

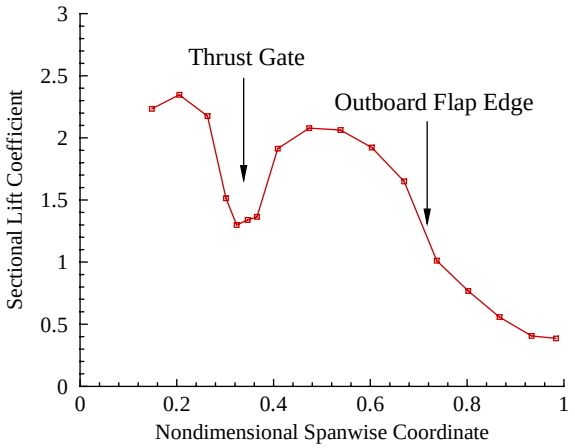

Fig. 14. Typical lift distribution of the DC-10 model aircraft with flow and high lift system conditions the same as those in Fig. 2.

From Fig. 14, the jump in C_L across the two measuring points is 0.6383 and the span-wise separation of the two points is $0.0673L$. For this model, the wing dimensions are

$$L = 1.2497\,\text{m} \quad \text{and} \quad b = 2.1654 \times 10^{-3}\,\text{m}. \tag{6.9}$$

Here b is given by the maximum value of the flap half thickness. For estimate purpose, we can assume that the chord-wise region where the vortex generates significant noise has varying values of b, from this maximum value to about 50% of it. With these, it is easy to show that

$$0.0197 \leqslant \Delta C_L \leqslant 0.0329. \tag{6.10}$$

From all these, the frequency prediction (6.7) becomes

$$5.7\,\text{kHz} \leqslant f_0 \leqslant 11.4\,\text{kHz}. \tag{6.11}$$

This prediction clearly covers the hump frequency shown in the test data and the frequency band is also consistent with that of the hump in the surface pressure spectra shown in Section 2. The predicted frequency is plotted in Fig. 15 as a function of the half flap thickness, normalized by its maximum value.

To examine the trends of the oscillation frequencies with the fence height, we now return to the case of non-zero h. In this case, we can avoid estimating U from the empirical formulas if we choose to work with the frequency ratio f/f_0, namely the frequency ratio between the cases of fenced and unfenced flap. By combining Eqs. (5.10) and (6.3), we have

$$\frac{f}{f_0} = \frac{U}{U_0}\frac{\omega}{192\sqrt{2}}, \tag{6.12}$$

where ω is the non-dimensional angular frequency defined by Eq. (5.10).

To find the quantity U/U_0, we note that the velocity far away from the side edge, namely, as $|z| \to \infty$, can be found from Eq. (4.2) as

$$u - \mathrm{i}v = -U/z'(\zeta) = -U/(a\zeta). \tag{6.13}$$

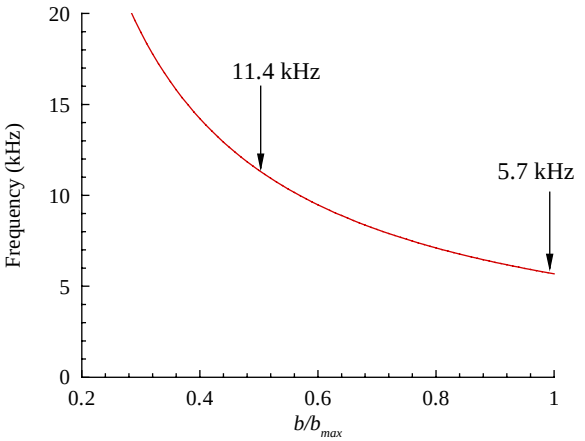

Fig. 15. Predicted frequency as a function of the flap half thickness, showing the consistency with test data discussed in Section 2.

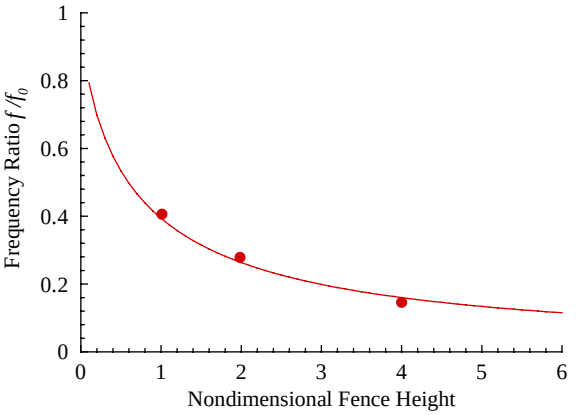

Fig. 16. Comparison between the predicted frequency ratio and teat data, as a function of the non-dimensional fence height: ——, prediction; ●, data.

The last step follows from applying the limit $|\zeta| \to \infty$ to the mapping Eq. (3.5). Also in this limit, it can be shown that

$$z = a\zeta^2/2. \tag{6.14}$$

By combining Eqs. (6.13) and (6.14), the tangential velocity on the flap lower surface far away from the side edge can be found to has an asymptotic form

$$u = \frac{U}{\sqrt{2}|a|^{1/2}|x|^{1/2}}. \tag{6.15}$$

This reveals the velocity decay law of the flow at large distance from the side edge. The inverse square root of the distance is typical of incompressible flows. From recent experiments on flap fences, it has been shown that fences affect the local flow in the side edge region, but do not have significant impact on the overall aerodynamic flow, especially away in regions away from the side edge. Thus, it stands to reason that the velocities far away from the side edge are essentially the same with or without fences. By using Eq. (6.15), this then leads to

$$U/U_0 = (a/a_0)^{1/2}, \tag{6.16}$$

where a_0 is the value of a in the baseline case of $h = 0$ and is given by Eq. (3.10). With the substitution of Eq. (6.16) into Eq. (6.12), we now have the prediction for the frequency ratio. Some results are shown in Fig. 16, where f/f_0 is plotted as a function of the non-dimensional fence height h. Also plotted in the figure are the results from the experiments discussed in Section 2. Clearly, the agreement between the predictions and the data is quite satisfactory.

7. Conclusions and discussions

In this paper, we have presented an analytical model for studying of the effects of flap fences on the flows in the flap side edge regions and their acoustic radiation. We have shown that the model

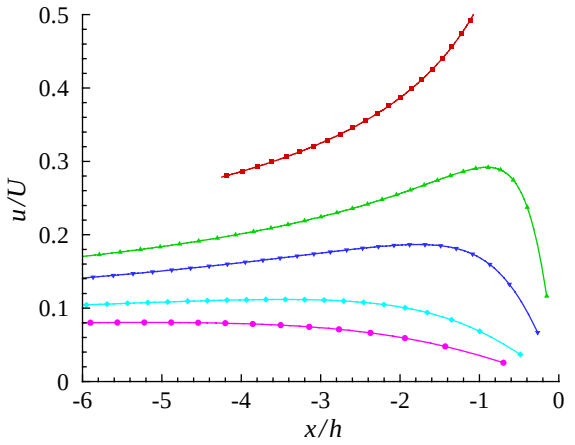

Fig. 17. Mean flow velocity on the lower flap surface for different fences, showing the trend of decreasing amplitude due to the blockage effect of the fences. -■-, 0; -▲-, $h = 0.5$; -▼-, $h = 1$; -◆-, $h = 2$; -●-, $h = 3$.

captures the major trends observed in experimental data. In particular, it shows that fences can achieve reduction of flap-related noise by shifting the source spectra downward in frequency. Analytical prediction for the frequency shift has been given and has been shown to agree with data quite satisfactorily.

It should be pointed out that the fences might also reduce noise by weakening the amplitudes of the source flow. This aspect is not discussed in this paper because our limited test data were not enough to derive any meaningful conclusions on this issue. Our analytical model, however, does reveal indications of this. The fences may be able to reduce the source strength by slowing down the local flow around the flap side edge, because of the blockage effects of the fences. Our simple model predicts that the flow velocity on the flap is indeed reduced by the fences, and the larger the fence height is, the lower the velocity. This is shown in Fig. 17, which plots the velocity distribution on the lower flap surface near the side edge for different fences. It is clear from the figure that the velocity is progressively reduced by the fences.

Acknowledgements

The work reported here is sponsored by the NASA Advanced Subsonic Technology (AST) Program, under the noise reduction element. The task monitor was Dr. M. G. Macaraeg of NASA LaRC, who has unfortunately passed away. Her support and encouragement are gratefully appreciated.

Appendix A. Nomenclature

C_L sectional lift coefficient
F auxiliary function associated with mapping

L wing semi-span
U velocity scale in mapping plane
U_0 values of U for baseline flap
U_∞ free stream velocity at infinity
W complex potential
a mapping constant
b flap halp thickness
f_i auxiliary functions in mapping ($i=1,2,3$)
f_0 vortex oscillation frequency for baseline flap
f vortex oscillation frequency for fenced flap
h flap fence height
p total pressure
p_0 constant mean pressure
p_s surface pressure on flap
q dynamic head
s flap fence thickness
t time
u velocity in flap span direction
v velocity normal to flap span direction
x co-ordinate in flap span direction
y co-ordinate normal to flap span direction
z complex co-ordinate ($=x+\mathrm{i}y$)
z_0 complex location of equilibrium vortex
Z_n complex locations of flap side edge vertices
Γ_0 strength of equilibrium vortex
β parameter associated with mapping
ε perturbation displacement of equilibrium vortex
γ_0 vorticity distribution in wing span direction
λ,μ locations of flap fence edges in mapping plane
ρ_0 constant mean density
ω angular frequency of vortex oscillation
ζ co-ordinate in mapping plane ($=\xi+\mathrm{i}\eta$)

References

[1] J.C. Hardin, Noise radiation from the side edges of flaps, *American Institute of Aeronautics and Astronautics Journal* 18 (5) (1980) 549–552.
[2] S.A. McInerny, W.C. Meecham, P.T. Soderman, An experimental investigation of wing tip turbulence with applications to aerosound, AIAA Paper 86-1918, 1986.
[3] D.G. Crighton, Airframe noise, *Aeroacoustics of Flight Vehicles: Theory and Practice*, NASA RP-1258, Vol. 1, 1991, pp. 391–447.
[4] Y.P. Guo, Prediction of flap edge noise, AIAA Paper 99-1804, 1999.
[5] T.F. Brooks, W.M. Humphreys, Flap-edge aeroacoustic measurements and predictions, *Journal of Sound and Vibration* 261 (2003) 31–74.

[6] J.C. Ross, B.L. Storms, H. Kumagai, Aircraft flyover noise reduction using lower-surface flap-tip fences, NASA CDTM-21006, 1995.
[7] B.L. Storms, T.T. Takahashi, W.C. Horne, J.C. Ross, R.P. Dougherty, J.R. Underbrink, Flap-tip treatments for the reduction of lift-generated noise, NASA CDTM-21006, 1996.
[8] Y.P. Guo, M.C. Joshi, Noise characteristics of aircraft high lift systems, *American Institute of Aeronautics and Astronautics Journal* 41 (7) (2003) 1247–1256.
[9] Y.P. Guo, P. Bent, K. Yamamoto, M.C. Joshi, Surface pressure fluctuations on aircraft high lift system and their correlation with far field noise, *Journal of Fluid Mechanics* 415 (2000) 175–202.
[10] M.R. Khorrami, B.A. Singer, R.H. Radeztsky, Reynolds averaged Navier–Stokes computations of a flap side-edge flow field, AIAA Paper 98-0768, 1998.
[11] K.R. Meadows, T.F. Brooks, W.M. Humphreys, W.H. Hunter, C.H. Gerhold, Aeroacoustic measurements of a wing flap configuration, AIAA Paper 97-1595, 1997.
[12] J.A. Hayes, W.C. Horne, P.T. Soderman, P.H. Bent, Airframe characteristics of a 4.7% scale DC-10 model, AIAA Paper 97-1594, 1997.